RuO2-CeO2 lattice matching strategy enables robust water oxidation electrocatalysis in acidic media via two distinct oxygen evolution mechanisms

Journal:	*ACS Catalysis*
Manuscript ID	cs-2023-06182t.R2
Manuscript Type:	Article
Date Submitted by the Author:	n/a
Complete List of Authors:	Song, Haoqiang; Zhengzhou University, College of Chemistry Yong, Xue; University of Sheffield, Chemistry Waterhouse, Geoffrey; University of Auckland, School of Chemical Sciences Yu, Jingkun; Zhengzhou University, College of Chemistry Wang, Hao; Zhengzhou University, College of Chemistry Cai, Jinmeng; Zhengzhou University, College of Chemistry Tang, Zhiyong; National Center for Nanoscience and Nanotechnology Yang, Bai; Jilin University, Chemistry Chang, Jiangwei; Zhengzhou University, College of Chemistry Lu, Siyu; Zhengzhou University, College of Chemistry

RuO_2-CeO_2 lattice matching strategy enables robust water oxidation electrocatalysis in acidic media via two distinct oxygen evolution mechanisms

Haoqiang Song[1,‡] , Xue Yong[2,‡], Geoffrey I.N. Waterhouse[3], Jingkun Yu[1], Hao Wang[1], Jinmeng Cai[1], Zhiyong Tang[4], Bai Yang[5], Jiangwei Chang[1,*], Siyu Lu[1,*]

[1]College of Chemistry, Zhengzhou University, Zhengzhou 450000, China.

[2]Department of Chemistry, The University of Sheffield, Brook Hill, Sheffield S3 7HF, United Kingdom.

[3]School of Chemical Sciences, The University of Auckland, Auckland 1142, New Zealand.

[4]CAS Key Laboratory of Nanosystem and Hierarchical Fabrication, CAS Center for Excellence in Nanoscience, National Center for Nanoscience and Technology, Beijing 100190, China.

[5]State Key Laboratory of Supramolecular Structure and Materials, College of Chemistry, Jilin University, Changchun 130012, China.

KEYWORDS. ruthenium dioxide, cerium dioxide, acidic water oxidation, oxygen evolution mechanism, lattice strain

ABSTRACT: The discovery of acid-stable and highly active electrocatalysts for the oxygen evolution reaction (OER) is crucial in the quest for high-performance water-splitting technologies. Herein, a heterostructured RuO_2-CeO_2 electrocatalyst was constructed using a lattice-matching strategy. The interfacial Ru-O-Ce bridge structure provided a channel for electron transfer between Ru and Ce, creating lattice stress that distorts the local structure of RuO_2. The resulting RuO_2-CeO_2 catalyst exhibited attractive stability with negligible decay after 1000 h of OER in 0.5 M H_2SO_4, along with high activity with an overpotential of only 180 mV at 10 mA cm^{-2}. *In-situ* attenuated total reflectance surface-enhanced infrared absorption spectroscopy (ATR-SEIRAS), *in-situ* differential electrochemical mass spectrometry (DEMS), and density functional theory (DFT) calculations were used to reveal that the interface and non-interface RuO_2 sites enabled an oxide path mechanism (OPM) and the enhanced adsorbate evolution mechanism (AEM-plus), respectively, during the OER. The simultaneous and independent OER pathways accessible by lattice matching guides improved electrocatalyst design for the OER in acidic media.

INTRODUCTION

Decarbonizing the global energy sector requires the rapid growth of a green hydrogen economy[1-3]. Electrocatalytic water splitting is widely considered the best approach for producing hydrogen at scale to support a green hydrogen energy infrastructure, with hydrogen ideally being produced from electricity generated by solar photovoltaics, wind turbines, or hydroelectric turbines[4-10]. The two mainstream water splitting technologies currently employed for hydrogen production are proton exchange membrane water electrolyzers (PEMWEs) and alkaline water electrolyzers. Compared to alkaline water electrolysis, PEMWEs offer many advantages including higher energy efficiency, higher current densities, and a purer hydrogen product[11-12].

However, a strongly acidic working environment necessitates the use of noble metal catalysts in commercial PEMWEs. For instance, platinum is typically employed for the hydrogen evolution reaction (HER) at the cathode, while iridium is used for the oxygen evolution reaction (OER) at the anode[13-15]. Unfortunately, this reliance on noble metals catalysts impedes the widespread adoption of this technology[8, 16-17]. The energy barrier associated with OER, which involves four-electron transfer steps, is much higher than that of the HER, which involves only two electron transfer steps. Consequently, PEMWEs typically use 5 times more iridium at the anode relative to platinum at the cathode to achieve optimal performance. Therefore, a primary focus for advancing PEMWE technology is the discovery of highly active, stable, and acid-resistant non-iridium OER electrocatalysts[18-20].

RuO_2 is widely considered the most promising alternative to IrO_2 for acidic OER, due ruthenium's higher earth abundance and good OER activity (higher than that of IrO_2). However, RuO_2-based electrocatalysts suffer from instability in acidic electrolytes due to the leaching of ruthenium[9, 21-25].

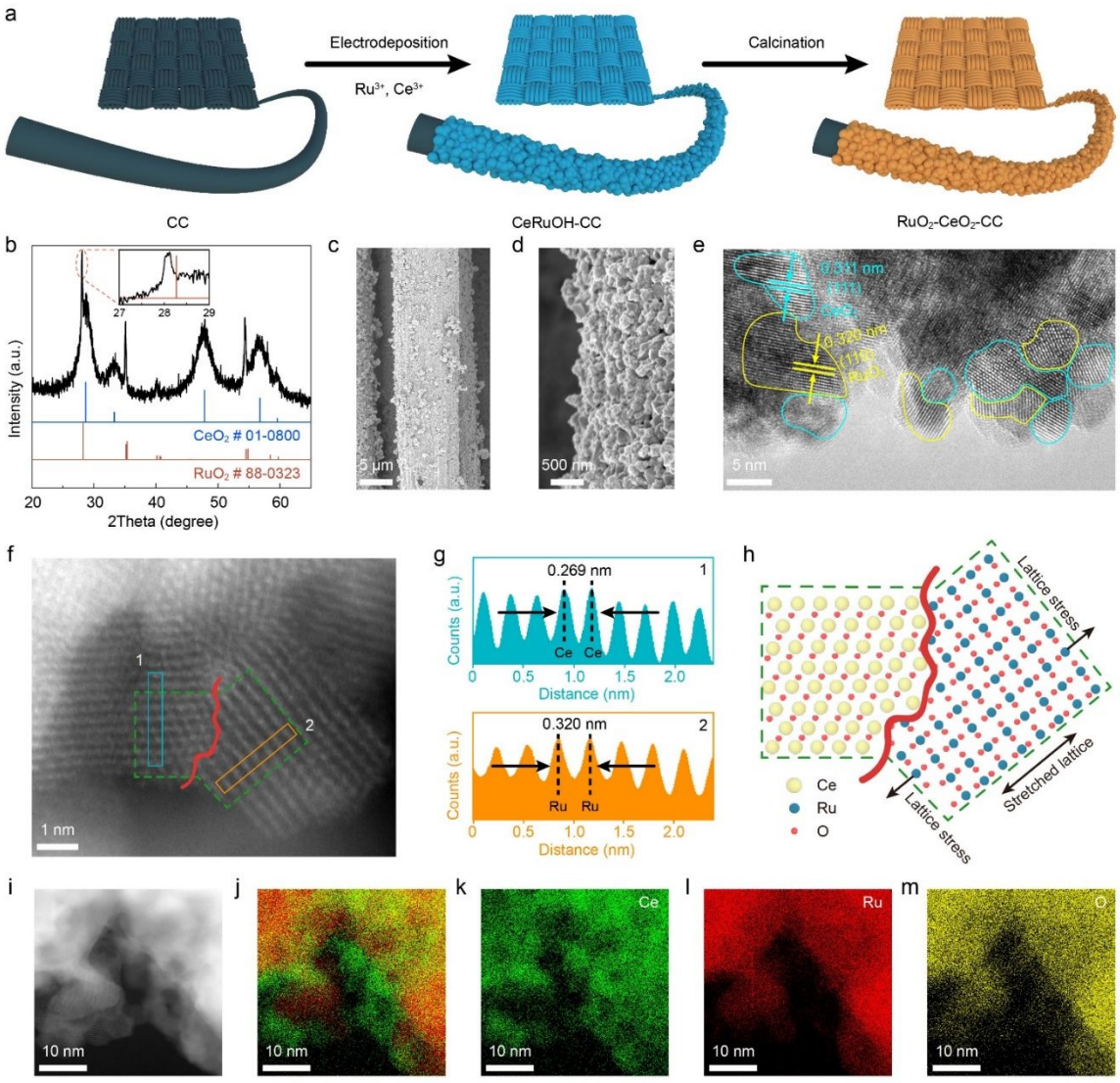

Figure 1. Morphological and structural characterizations. (a) Schematic illustration of the synthesis of the RuO_2-CeO_2-CC catalyst. (b) XRD pattern (Inset: magnified view of the RuO_2 peak in RuO_2-CeO_2, which has a slightly lower 2θ angle compared to typical RuO_2(110)). (c, d) SEM images, (e) TEM image, (f) aberration-corrected HAADF-STEM image. (g) atomic model of RuO_2-CeO_2 corresponding to the green framed region in f. (h) Line-scanning intensity profiles corresponding to the blue and yellow boxes in f. (i-m) STEM image and elemental mapping images for RuO_2-CeO_2.

To overcome this limitation, various strategies including heterostructure engineering, defect engineering, and doping have been employed to improve both electrocatalyst activity and durability[26-29]. For example, Ling *et al* demonstrated that by constructing a RuO_2/CoO_x interface, the stability and activity limits of RuO_2 can be overcome, resulting in high OER activity (240 mV at 10 mA cm^{-2}) and long-term stability (200 h) under neutral conditions[12]. Kim *et al* synthesized a Ni-doped metallic-core with an oxide-shell of Ru catalyst through a thermal acid treatment, with the resulting electrocatalyst exhibiting outstanding activity with an OER overpotential of only 184 mV at 10 mA cm^{-2} and stability for about 200 h in acidic media[30]. While significant advances have been made to improve the stability of RuO_2-based electrocatalysts for acidic OER, performance still falls well short of practical requirements. More robust RuO_2-based acid-resistant OER catalysts need to be found.

In recent years, CeO_2 has emerged as an excellent support material and co-catalyst in the field of electrocatalysis, often enhancing both catalyst stability and activity[31-33]. This can be attributed to the Ce^{3+}/Ce^{4+} redox properties and oxygen storage properties of CeO_2, which in RuO_2-CeO_2 heterostructures can be used to prevent the excessive oxidation of Ru (i.e. electron transfer from Ce^{3+} prevents Ru over-oxidation and dissolution)[34-37]. Engineering electrocatalysts with RuO_2-CeO_2 heterostructures thus holds great promise in the development of efficient and acid-stable OER electrocatalysts.

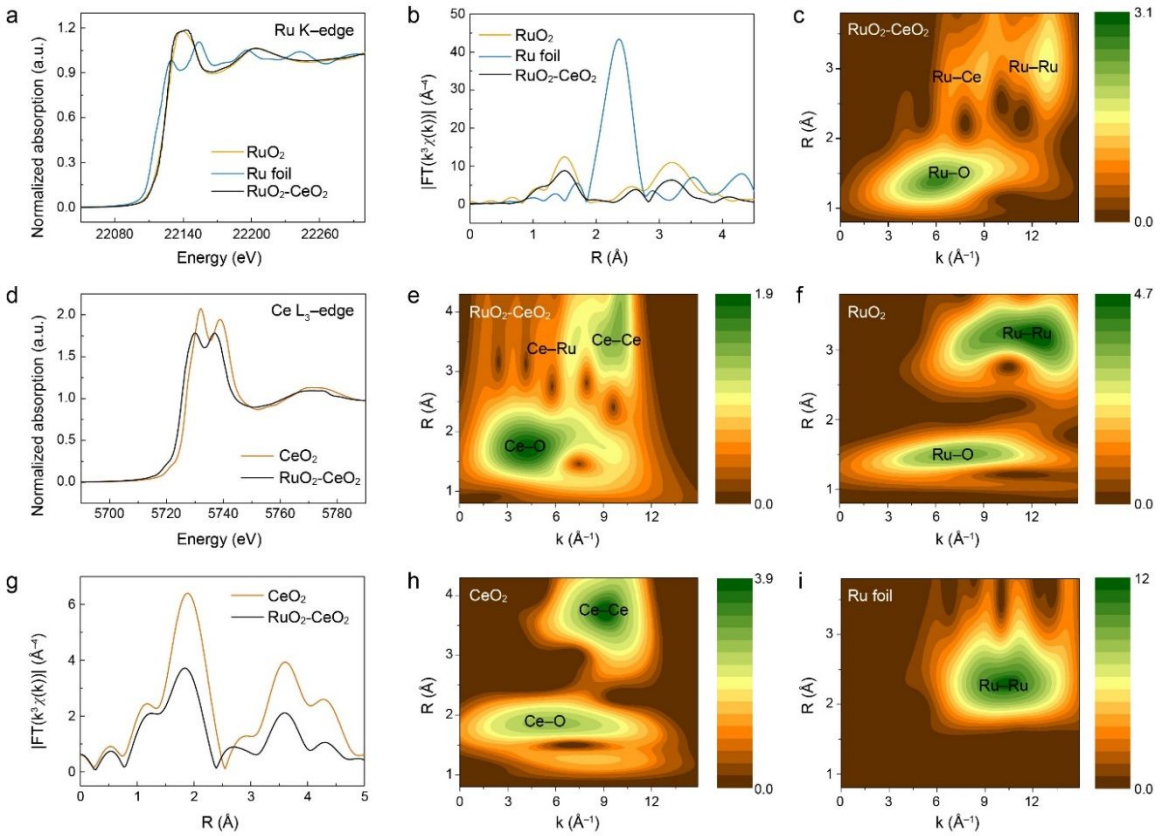

Figure 2. Structural analysis of the catalysts. (a) Ru *K*-edge XANES and (b) Ru *K*-edge EXAFS spectra for RuO_2-CeO_2, commercial RuO_2, and Ru foil. Wavelet transform of Ru *K*-edge EXAFS data of (c) RuO_2-CeO_2 (f) commercial RuO_2, and (i) Ru foil. (d) Ce L_3-edge XANES and (g) Ce L_3-edge EXAFS spectra of RuO_2-CeO_2, and CeO_2. Wavelet transform of Ce L_3-edge EXAFS data of (e) RuO_2-CeO_2, and (h) CeO_2.

Lattice stress strategies that can adjust the d-band center shift and optimize the binding properties of intermediates have been widely used in electrocatalytic systems such as oxygen reduction reaction and CO_2 reduction reaction, but they are rarely mentioned in acidic OER reaction systems. It is worth mentioning that the process of forming a heterostructure through lattice matching between RuO_2 and CeO_2 will induce lattice strain, which will also be a complement to the application of lattice stress in acidic OER reaction systems[38-43]. Moreover, most reports today focus on the study of a single OER path, with there being a lack of understanding about whether the OER paths at heterojunction interfaces and non-interface RuO_2 sites are the same.

Herein, RuO_2 and CeO_2 nanoparticle heterostructures were grown on carbon cloth (RuO_2-CeO_2-CC) using a simple electrodeposition-calcination method. The resulting RuO_2-CeO_2-CC electrocatalyst exhibits remarkable OER catalytic activity in an electrochemical three-electrode system in acid, requiring an overpotential of only 180 mV to achieve a current density of 10 mA cm^{-2} (based on geometric area) in 0.5 M H_2SO_4. Furthermore, RuO_2-CeO_2-CC demonstrates outstanding long-term durability over 1000 h. The different OER mechanisms at the heterojunction interface and non-interface of RuO_2-CeO_2 heterostructures fabricated by lattice matching were investigated using *in-situ* ATR-SEIRAS, *in-situ* DEMS, and DFT calculations. At the non-interfacial RuO_2 sites, an enhanced version of the adsorbate evolution mechanism (AEM-plus) pathway was observed, with lattice strain caused by lattice matching distorting the structure of RuO_2 and activating the O atoms near the active site to behave and a proton acceptor and lower the energy barrier for the formation of *OOH. Conversely, an oxide path mechanism (OPM) occurred at the RuO_2-CeO_2 interfaces, with electron transfer between Ru and Ce atoms through the Ru-O-Ce oxygen bridge producing a strong electronic coupling effect that directly connects dioxygen radicals at adjacent sites. This system offers a low overall reaction energy barrier for OER and fast kinetics. Furthermore, the Ru-O-Ce oxygen bridge acted to suppress Ru dissolution, giving the RuO_2-CeO_2-CC electrocatalyst remarkable stability during the OER under acidic conditions.

RESULTS AND DISCUSSION

Preparation and characterization of RuO_2-CeO_2-CC. As shown in Figure 1a, a two-step electrodeposition-calcination strategy was used to prepare the RuO_2-CeO_2-CC electrocatalyst. Initially, amorphous Ru and Ce compounds (oxide/hydroxide phases) were electrodeposited on the surface of the carbon cloth (RuCeOH-CC) in an electrolyte containing Ru and Ce ions. Subsequently, the obtained RuCeOH-CC was calcined to produce the RuO_2-CeO_2-CC electrocatalyst containing RuO_2 and CeO_2 nanoparticles with abundant RuO_2-CeO_2 interfaces supported on carbon cloth. Detailed information about the synthesis of RuO_2-CeO_2-CC is provided in the method section.

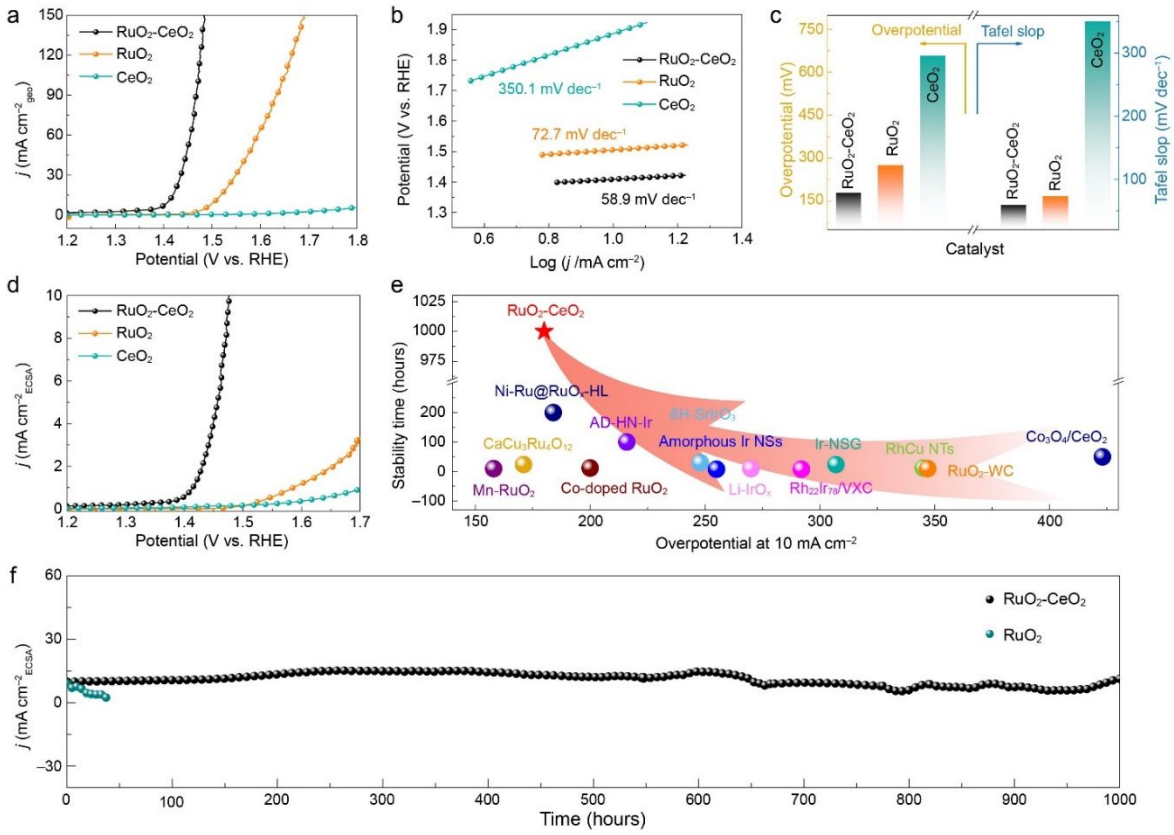

Figure 3. Electrochemical OER activity studies at 25 °C. (a) OER polarization curves, and (b) corresponding Tafel slopes for RuO_2-CeO_2-CC, CeO_2-CC and RuO_2-CC in 0.5 M H_2SO_4. The activity of each catalytic material was normalized to the geometric area. (c) Histograms of overpotentials at 10 mA cm^{-2}_{geo} and Tafel slopes for various catalysts. (d) OER polarization curves for RuO_2-CeO_2-CC, CeO_2-CC and RuO_2-CC in 0.5 M H_2SO_4. The activities of the catalytic materials were normalized to ECSA. (e) Comparison of the required overpotential to achieve 10 mA cm^{-2}_{geo} and stability for RuO_2-CeO_2-CC and other reported catalysts (Supplementary Table S1) during OER in acidic media. (f) Time-dependent current density curves for RuO_2-CeO_2-CC and RuO_2-CC at 1.41 V versus RHE and commercial RuO_2-CC at 1.51 V versus RHE.

The X-ray diffraction (XRD) pattern for RuO_2-CeO_2 showed peaks due to CeO_2 (JCPDS No.01-0800) and RuO_2 (JCPDS No. 88-0323). The CeO_2 peaks were broad suggesting small nanoparticles, whereas the RuO_2 peaks were much sharper suggesting the presence of larger particles. The RuO_2 peaks for RuO_2-CeO_2-CC were at slightly lower 2θ angles (shifted by ~0.2°) compared to those typically observed for RuO_2, suggesting the unit cell of RuO_2 had expanded slightly. This was likely due to the presence of the abundant RuO_2-CeO_2 heterostructures causing slight distortions of the RuO_2 lattice.

Next, the morphology of the RuO_2-CeO_2-CC electrocatalyst was investigated by scanning electron microscopy (SEM). The SEM images (Figure 1c-d) confirmed the presence of typical RuO_2 and CeO_2 nanoparticles firmly connected to the carbon cloth, which helped to explain the excellent stability of RuO_2-CeO_2-CC during OER tests (see below). Further morphological and structural investigations was carried out using transmission electron microscopy (TEM), and high-resolution TEM (HRTEM). The TEM analyses revealed abundant RuO_2-CeO_2 heterostructures the electrocatalyst, with the RuO_2 and CeO_2 nanoparticles in intimate contact (Figure 1e; Supplementary Figure S1). Lattice fringe spacings were used to identify the individual nanoparticles. As shown in Figure 1e, the lattice spacings of 0.311 nm correspond to the (111) plane of cubic CeO_2, whereas fringes with a spacing of 0.320 nm were readily indexed to the (110) plane of orthorhombic RuO_2 (typically ~0.315 nm). The slightly larger lattice spacing here for the RuO_2(111) accords well with the XRD findings (i.e. slight RuO_2 lattice expansion caused by the presence of contacting CeO_2 nanoparticles). To obtain deeper insight into the atomic structure of RuO_2-CeO_2, aberration-corrected high-angle annular dark-field scanning transmission electron microscopy (HAADF-STEM) was employed. In the HAADF-STEM of RuO_2-CeO_2, interconnected lattice fringes with spacings on 0.269 nm and 0.320 nm were observed, and assigned to CeO_2(200) and distorted RuO_2(110) planes, respectively (Figure 1f-h). HAADF-STEM verified intimate heterointerfaces existed between the RuO_2 and CeO_2 nanoparticles in RuO_2-CeO_2. The distinct boundaries were also confirmed by HAADF-STEM elemental mapping studies (Figure 1i-m).

To further explore the electronic structure and local coordination environment of Ru and Ce cations in the nanocomposites, X-ray absorption spectroscopy data for RuO_2-CeO_2 powder was collected at the Ru *K*-edge and Ce L_3-edge. Ru foil, commercial RuO_2, and CeO_2 were used as reference samples. The oxidation state of Ru in RuO_2-CeO_2 powder was established form the Ru *K*-edge X-ray absorption near-edge fine structure (XANES) region, while the local coordination information was obtained from the extended X-ray absorption

fine structure (EXAFS) region. The Ru *K*-edge absorption edge position in the XANES region for RuO_2-CeO_2 (Figure 2a) was similar to that of the RuO_2 reference sample, confirming the predominance of Ru^{4+}. This was not surprising, since XAS is a bulk measurement with Ru atoms in RuO_2-CeO_2 likely to be unaffected by the Ru-O-Ce interfaces[39]. The Ru *K*-edge EXAFS spectrum is R-space (Figure 2b) showed two distinct peaks 1.48 Å (first shell) and 3.19 Å (in the second shell), which could readily be assigned to Ru-O and Ru-Ru/Ce scattering paths (as confirmed by peak fitting routines). The Ru-O scattering path for RuO_2-CeO_2 was similar to that of the RuO_2 reference sample. A wavelet transform (WT) analysis was next applied to the EXAFS data, thus enabling the contributions of different scattering paths to the EXAFS signal of RuO_2-CeO_2 to be explored in further detail. In Figure 2c, three major maxima were observed at k = ~6.1 $Å^{-1}$, ~8.8 $Å^{-1}$, and ~12.8 $Å^{-1}$, respectively, which are assigned to the first coordination shell i.e. the Ru-O scattering path (k ~6.1 $Å^{-1}$) and the second coordination shell of the Ru-Ru/Ce scattering path (k ~8.8 $Å^{-1}$, and k ~12.8 $Å^{-1}$), respectively. By comparison with the WT EXAFS data for RuO_2, we assign the feature at k ~8.8 $Å^{-1}$ to Ru-O-Ce, and the other feature at k ~12.8 $Å^{-1}$ to Ru-O-Ru. These assignments were further confirmed by subsequent WT analysis of the Ce L_3-edge data for RuO_2-CeO_2.

In the Ce *K*-edge XANES spectrum of RuO_2-CeO_2 powder (Figure 2d), the absorption edge was located at lower photon energies compared with the reference CeO_2 material. Further, the white line peak intensity of RuO_2-CeO_2 powder was lower than that of the reference CeO_2 sample, indicating that more electrons were concentrated at the Ce sites in RuO_2-CeO_2 (i.e. RuO_2-CeO_2 contained more Ce^{3+} sites, presumably via electron transfer from RuO_2). The Ce *K*-edge EXAFS spectrum in R-space (Figure 2g) showed main peaks at 1.5 Å and 3.5 Å, which could readily be assigned to Ce-O (first coordination shell) and Ce-Ce/Ru (second shell), respectively. The WT contour map for RuO_2-CeO_2 showed three intensity maxima at 4.2 $Å^{-1}$, 7.3 $Å^{-1}$, and 9.9 $Å^{-1}$, which were assigned to Ru-O, Ce-Ru, and Ce-Ce scattering paths, respectively (Figure 2e) by comparison with data collected for the CeO_2 reference sample (Figure 2h). This was consistent with the WT EXAFS data for Ru in RuO_2-CeO_2, verifying the presence Ru-O-Ce oxygen bridges in RuO_2-CeO_2. The electronic states in the as-prepared RuO_2-CeO_2 were further probed using X-ray photoelectron spectroscopy (XPS). As shown in Figure S2 (Supplementary), XPS confirmed the presence of Ru, Ce, and O in the RuO_2-CeO_2-CC catalyst surface (along with some C, in the form of adventitious hydrocarbons). The main Ce $3d_{5/2}$ XPS peak for RuO_2-CeO_2-CC was shifted to lower binding energy (882.3 eV) compared with that of the CeO_2-CC (883.2 eV) reference sample, again suggesting a lower average Ce valence in RuO_2-CeO_2-CC. This is consistent with the Ce L_3-edge XANES data for the same samples (Supplementary Figure S3-S4). Taken together, the XPS and XANES data suggest electronic coupling between the RuO_2 and CeO_2 nanoparticles in RuO_2-CeO_2-CC via the interfacial Ru-O-Ce oxygen bridges (with charge transfer from Ru to Ce).

Electrocatalytic performance for RuO_2-CeO_2-CC. A standard three-electrode system was adopted to investigate the OER performance of the different catalysts in a 0.5 M H_2SO_4 electrolyte. In this system, the performance of RuO_2-CeO_2-CC was compared with CeO_2-CC and commercial RuO_2 (i.e. RuO_2-CC). Among the three catalysts, RuO_2-CeO_2-CC delivered excellent OER performance (Figure 3a). In the OER reaction, to achieve current densities of 10, 50, and 100 mA cm^{-2}_{geo} with respect to the geometric area (1 cm^2), RuO_2-CeO_2-CC required overpotentials of only 180, 220, and 242 mV, respectively. In contrast, CeO_2-CC (658 mV) and RuO_2-CC (275 mV) require much larger overpotentials to reach a current density of 10 mA cm^{-2}_{geo}. RuO_2-CeO_2-CC delivered a low Tafel slope of only 58.9 mV dec^{-1} for OER (Figure 3b), much lower than the corresponding Tafel slopes for CeO_2-CC (350.1 mV dec^{-1}) and RuO_2-CC (64.4 mV dec^{-1}). The data confirmed fast OER kinetics on RuO_2-CeO_2-CC. Figure 3c compares the overpotentials (at 10 mA cm^{-2}_{geo}) and Tafel slopes for the various catalysts tested in this work. The comparison demonstrates that the Ru-O-Ce oxygen bridges in RuO_2-CeO_2-CC greatly reduce the OER reaction barrier. In general, the electrochemically active surface area (ECSA) of an electrocatalyst is proportional to the double-layer capacitance (C_{dl}) and considered an important indicator of the number of surface active sites. The C_{dl} values calculated for the various catalysts followed the order: RuO_2-CC (134.2 mF cm^{-2}) > RuO_2-CeO_2-CC (30.8 mF cm^{-2}) > CeO_2-CC (7.0 mF cm^{-2}) > CC (2.5 mF cm^{-2}) (Supplementary Figure S7-S10). The commercial RuO_2 sample offered the highest ECSA value, suggesting it highest abundance of active sites. However, RuO_2-CeO_2-CC delivered best OER catalytic performance. Hence, the ECSA was only one of the factors affecting the OER activity of the electrocatalysts (and not the most important), which was confirmed in further studies examining the intrinsic activity of the electrocatalysts. By normalizing the OER activities for RuO_2-CeO_2-CC, CeO_2-CC and RuO_2-CC against the ECSA values (Figure 3d), it was found that RuO_2-CeO_2-CC delivered the highest intrinsic activity among the three electrocatalysts in acidic media.

Stability is a further important consideration when applying OER catalysts in large-scale applications. Thus, the time-dependent current density curves were collected for RuO_2-CeO_2-CC in 0.5 M H_2SO_4 to assess its stability. RuO_2-CeO_2-CC maintained excellent OER activity over 1000 h at a current density of 10 mA cm^{-2}_{geo} and an applied potential of 1.41 V vs. RHE (Figure 3f), showing remarkable OER stability. In contrast, the performance of the RuO_2-CC electrocatalyst declined rapidly under the same testing conditions. The outstanding stability of RuO_2-CeO_2 puts a spotlight on the critical role of Ru-O-Ce heterointerfaces and RuO_2 lattice stress in preventing Ru dissolution during OER (as discussed below). Figure 3e and Supplementary Table 1 compare the performance of RuO_2-CeO_2-CC with previously reported OER electrocatalysts in acidic media. In terms of both activity and long-term stability, RuO_2-CeO_2-CC is far superior to the other OER electrocatalysts reported to date. Moreover, after 1000 h of continuous OER operation, SEM, TEM, and XRD characterization studies verified that RuO_2-CeO_2-CC maintained its initial morphology and structure (Supplementary Figure S11-S13).

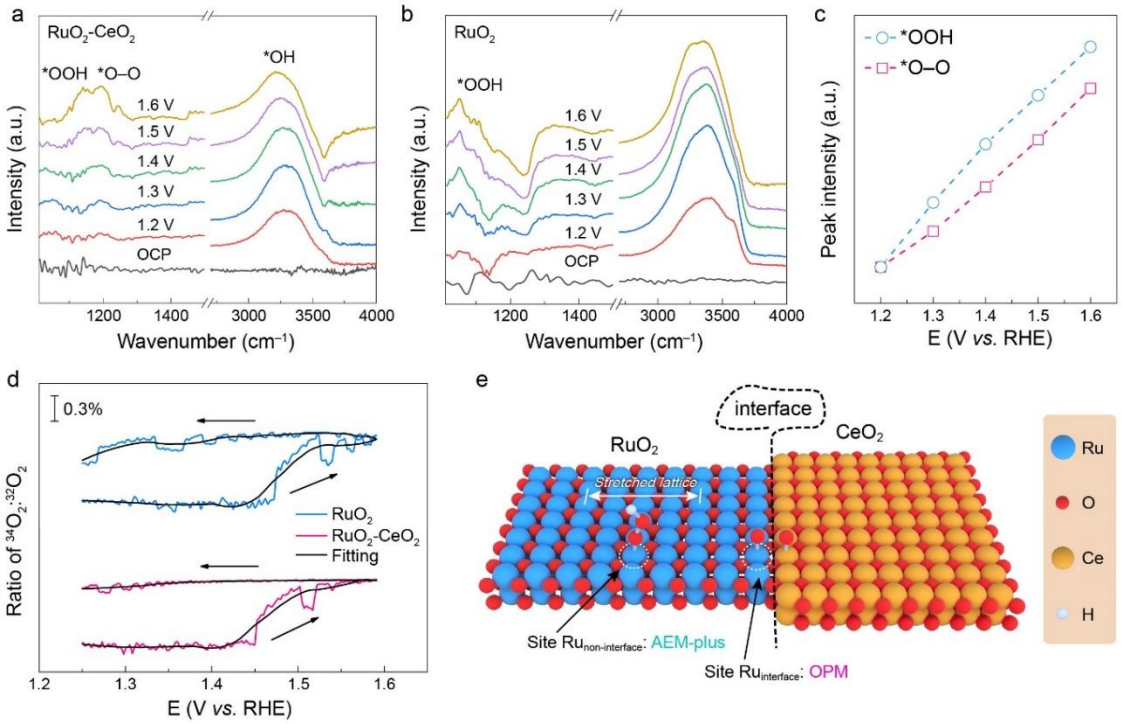

Figure 4. OER reaction mechanism investigations. *In-situ* ATR-SEIRAS spectra at various applied potentials for (a) RuO_2-CeO_2 and (b) RuO_2. Catalytic sites are indicated by the symbol *. (c) Potential dependence of the intensity of the ATR-SEIRAS peaks for *OOH and *O–O for RuO_2-CeO_2. (d) Ratio of $^{34}O_2$:$^{32}O_2$ measured by DEMS as a function of the applied potential. (e) Schematic diagram of the OER active sites and pathways for RuO_2-CeO_2 catalyst at the interface and non-interface.

Supplementary Figure S14 shows the concentration of Ru in the electrolyte as a function of time during the long-term OER tests for RuO_2-CeO_2-CC and RuO_2-CC. After 50 h of operation, the dissolved concentration of Ru in the electrolyte was 148 ppb for RuO_2-CC. For RuO_2-CeO_2-CC, the Ru dissolution rate was much lower and showed no change after 10 h of operation. Clearly, the RuO_2-CeO_2 heterostructure inhibited the dissolution of RuO_2 during acidic OER. The electrochemical data shows that RuO_2-CeO_2-CC is an outstanding electrocatalyst for OER in acidic media.

OER Mechanism and Origins of Enhanced Activity. *In-situ* ATR-SEIRAS was employed to investigate the OER mechanisms over RuO_2-CeO_2 and commercial RuO_2. The method allows identification of the potential-dependent reaction intermediates formed surface of catalytic materials during OER. For the measurements, each catalyst was drop-coated onto gold-coated silicon prisms. The catalyst-decorated prisms then assembled in the *in-situ* electrochemical cell of the FTIR system. Figure 4a shows *in-situ* ATR-SEIRAS spectra for RuO_2-CeO_2 at different working potentials. In addition to an absorption peak at 3261 cm^{-1} attributed to an O-H stretching mode of *OH, two distinct absorption peaks were seen at 1146 cm^{-1} and 1192 cm^{-1}, corresponding to O-O stretching vibrations of *OOH and *O–O adsorbed on the catalyst surface, respectively[18-19]. Recent reports suggest that the presence of *OOH indicates that the OER process involves an AEM pathway, whereas the occurrence of *O–O species suggests a lattice-oxygen-mediated mechanism or alternatively an OPM[45-48]. In contrast, the *in-situ* ATR-SEIRAS spectra for RuO_2 showed only absorption peaks at 3371 cm^{-1} and 1049 cm^{-1} (Figure 4b), associated with *OH and *OOH species. The difference in the *OOH absorption peak position between RuO_2 and RuO_2-CeO_2 may be due to the difference in the vibration frequency of *OOH caused by the stretching of the RuO_2 lattice in the RuO_2-CeO_2 heterojunction. No peaks associated with *O–O were observed for the RuO_2 catalyst. The data indicates that OER on RuO_2 follows an AEM-type pathway, consistent with literature findings[18, 47]. It is noteworthy that both the *OOH peak and *O–O peak intensities for RuO_2-CeO_2 (Figure 4a) increased linearly with the applied voltage (Figure 4c), indicating that the OER catalytic pathways were potential independent[44]. These *in-situ* data suggests that, compared with RuO_2, the heterostructured RuO_2-CeO_2 catalyst simultaneously enables multiple OER pathways, with one pathway occurring at the RuO_2-CeO_2 interface and a more traditional AEM pathway occurring on non-interface Ru sites. To further elucidate the OER mechanism on the RuO_2-CeO_2 catalyst, we measured its electrocatalytic activity in electrolytes of different pH. The current density of RuO_2-CeO_2 at 1.45 V vs. RHE showed a noticeable decrease on increasing the pH from 0 to 1 (Supplementary Figure S15-S17), which indicates that a non-coordinated proton-electron transfer step exists in the OER process of RuO_2-CeO_2. The pH dependence of OER activity strongly illustrates that the RuO_2-CeO_2 process of OER is carried out through multiple pathways simultaneously, that is, in addition to the AEM pathway carried out at RuO_2, there are other OER pathways occurring[5, 20].

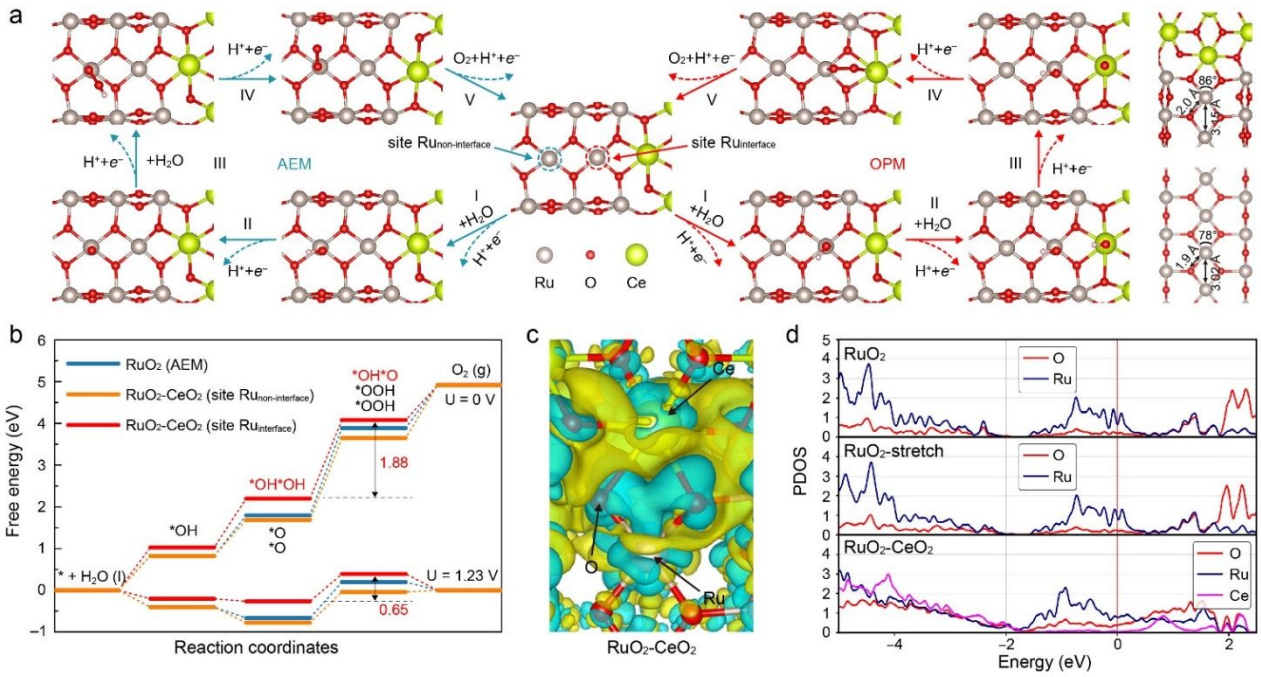

Figure 5. DFT calculations of the OER mechanism. (a) The AEM and OPM paths of OER on a RuO_2-CeO_2 catalyst. The Ru site involved in AEM and OPM on RuO_2-CeO_2 is labeled as $Ru_{non\text{-}interface}$ and $Ru_{non\text{-}interface}$, respectively. Right: Comparison of crystal structure models of RuO_2-CeO_2 and RuO_2 on the right, where lattice adaptation affects the angles and inter-atomic distances in the crystal structure. (b) Free energy diagrams for the preferred OER paths on the surfaces of RuO_2 and RuO_2-CeO_2. (c) Differential charge density analysis of RuO_2-CeO_2. The blue and yellow shaded areas correspond to regions of electron density accumulation and depletion, respectively. (d) PDOS of Ru 4*d*, and O 2*p*, for RuO_2, RuO_2-stretch and RuO_2-CeO_2.

Next, *in-situ* DEMS was applied to gain further insights about the OER mechanisms over RuO_2-CC and RuO_2-CeO_2-CC. Initially, the electrocatalysts were labeled with ^{18}O through electrochemical CV in a $H_2{}^{18}O$/0.5 M H_2SO_4 solution (with evolved $^{32}O_2$, $^{34}O_2$ and $^{18}O_2$ being monitored). If lattice oxygen participated in the isotope exchange process, ^{18}O would be incorporated in the catalyst surface. Next, an ample amount of $H_2{}^{16}O$ was used to wash the catalysts to remove any surface adsorbed $H_2{}^{18}O$. Subsequently, the washed catalysts were subjected to electrochemical CV and DEMS measurements in a $H_2{}^{16}O$/0.5 M H_2SO_4 solution and the evolved $^{32}O_2$, $^{34}O_2$ and $^{18}O_2$ monitored by mass spectrometry. Supplementary Figure S18-S19 shows the DEMS signals of the O_2 produced during the initial ^{18}O labeling process. Both $^{34}O_2$ and $^{36}O_2$ were produced in the CV cycles for RuO_2-CC and RuO_2-CeO_2-CC. The generation of $^{34}O_2$ was likely due to some initially adsorbed ^{16}O species (water or hydroxyl) on the catalyst surface. Four consecutive CV cycles were then conducted in $H_2{}^{18}O$/0.5 M H_2SO_4 in an effort to label ^{18}O on the catalyst surface. The catalysts were then washed with $H_2{}^{16}O$, then subjected to continuous CV cycles in $H_2{}^{16}O/H_2SO_4$ electrolyte. ^{18}O introduced in the catalyst lattice could potentially either couple with each other to generate $^{36}O_2$, or couple with $H_2{}^{16}O$ in the electrolyte to generate $^{34}O_2$. DEMS results for RuO_2 and RuO_2-CeO_2 are presented in Supplementary Figure S20-S21. Both catalysts gave a very weak $^{34}O_2$ signal, no $^{36}O_2$ signal and a very strong $^{32}O_2$ signal, with the $^{34}O_2$:$^{32}O_2$ ratio for RuO_2 and RuO_2-CeO_2 changing in the same manner as the OER potential was changed (Figure 4d). Therefore, the DEMS data suggest that lattice oxygen was not important in the OER process on either RuO_2-CC or RuO_2-CeO_2-CC[5]. The observation of a weak $^{34}O_2$ signal for each catalyst in the DEMS experiments was likely due to adsorbed $H_2{}^{18}O$ of ^{18}OH formed during the labeling step. It is widely accepted that the OER pathway on RuO_2 does not involve lattice oxygen, consistent with the findings here. Combining the results of electrochemical activity tests and *in-situ* ATR-SEIRAS experiments, we postulate that OPM pathway occurs at RuO_2-CeO_2 interfaces in RuO_2-CeO_2-CC, whereas AEM pathway occurs on the RuO_2 nanoparticles spatially-distanced from the interfaces (Figure 4e).

DFT calculations were conducted to gain insight into the origin of the activity of RuO_2-CeO_2. We used the 110 rutile RuO_2 surface and the 100 CeO_2 surface to construct the RuO_2-CeO_2 structures. Four different interfaced structures were considered. The most stable one was selected for further OER analysis. In the most stable RuO_2-CeO_2 structures, the two surfaces aligned very well, forming an extended coordinatively unsaturated site (CUS) row and bridge row via Ru-O-Ce bonds (Supplementary Figure S22). Previous theoretical studies have recommended CUS Ru sites were the main OER active sites[18, 45]. CeO_2 not only induced charge transfer but also introduced lattice strain to RuO_2, playing an important role in tuning the geometrical and electronic structures of RuO_2. A significant charge transfer from Ru to Ce through the Ru-O-Ce bridge was observed (Figure 5c; Supplementary Figure S23). The difference in the electronic and oxidation states of Ru and Ce allowed the OPM path (Figure 5a). The RuO_2 portion in RuO_2-CeO_2 experiences a stretch of around 4% along the CUS rows, in good agreement with the experimental measurements. Simultaneously, the Ru-O bond undergoes stretching compared to the pristine RuO_2. To better understand the lattice strain effect, we conducted separate calculations for pristine (110) RuO_2, applying a 2% lattice strain along the CUS row. The results showed that lattice strain shifted the d band center from

–2.38 eV for pristine RuO_2 to –2.32 eV (Figure 5d). Such a difference could lead to variations in intermediate adsorption and eventually affect the OER overpotential.

Reaction profiles based on the four elementary steps of AEM and OPM for RuO_2 and RuO_2-CeO_2 are shown in Figure 5b. For pristine RuO_2, OER proceeded favorably via an AEM path, following four-proton-coupled electron transfer steps: $H_2O \rightarrow *OH \rightarrow *O \rightarrow *OOH \rightarrow O_2$. The formation of *OOH is the rate-determining step (RDS) with a large free energy barrier of 2.10 eV. Interestingly, for the RuO_2-CeO_2 catalyst, OER can simultaneously proceed via both AEM and OPM but at different sites (site $Ru_{non\text{-}interface}$ and site $Ru_{interface}$, respectively). At the interface, due to the charge transfer channel, and the different *OH adsorption ability, the dual-site OPM path was activated. The formation of *OH*O intermediate became the RDS, with a free energy barrier of only 1.88 eV, which lowers the overpotential to 0.65 eV. Furthermore, we found the $Ru_{non\text{-}interface}$ sites in RuO_2 in the RuO_2-CeO_2 catalyst become more active. The adsorption of *OH became even stronger due to the shift of the d-band center toward the Fermi level. Even so, the OER still proceeded favorably via the AEM pathway, since the formation of *OOH became easier with a free energy barrier of only 1.96 eV. Therefore, the formation of RuO_2-CeO_2 heterostructures significantly enhanced the OER performance. Since RuO_2-CeO_2 interfaces occupy only a small part of the RuO_2-CeO_2 catalyst, the lattice distortion of RuO_2 appears important for achieving enhanced OER performance.

CONCLUSIONS

This work aimed to address one of the critical bottlenecks in water splitting technologies (i.e. the need to develop efficient and acid-stable OER catalysts). We demonstrate that a heterostructured RuO_2-CeO_2-CC electrocatalyst prepared using a simple electrodeposition-calcination strategy demonstrates exceptional activity and stability during OER in acid media. RuO_2-CeO_2-CC required an overpotential of 180 mV to achieve a current density of 10 mA cm^{-2}_{geo} during OER in 0.5 M H_2SO_4, and negligible loss in activity over 1000 hours at 10 mA cm^{-2}_{geo}. Detailed mechanistic investigations revealed that the interface and non-interface sites of RuO_2-CeO_2 simultaneously carry out the OPM and AEM pathways respectively during the OER process. RuO_2 lattice distortions induced by CeO_2 promote the deprotonation of adsorbed *OH atoms near Ru sites, facilitating the stable adsorption of *OOH to lower the energy barrier of the AEM reaction path. In addition, the Ru and Ce atoms at the interface form a strong electronic coupling effect through the Ru-O-Ce oxygen bridge, which makes the direct coupling of dioxygen radicals favorable during the OER process. These findings demonstrate a simple strategy to enable simultaneous AEM and OPM pathways during the acidic OER. Results inform the design of highly active and stable acidic OER electrocatalysts, expediting the future growth of a Green Hydrogen Economy.

ASSOCIATED CONTENT

Supporting Information.

The Supporting Information is available free of charge via the Internet at http://pubs.acs.org.

Experimental section, computational detail, materials characterization, and figures and tables (PDF)

AUTHOR INFORMATION

Corresponding Authors

Jiangwei Chang − *College of Chemistry, Zhengzhou University, Zhengzhou 450000, China*; Email: jwchang2021@zzu.edu.cn

Siyu Lu − *College of Chemistry, Zhengzhou University, Zhengzhou 450000, China;* Email: sylu2013@zzu.edu.cn

Authors

Haoqiang Song − *College of Chemistry, Zhengzhou University, Zhengzhou 450000, China*

Xue Yong − *Department of Chemistry, The University of Sheffield, Brook Hill, Sheffield S3 7HF, United Kingdom*

Geoffrey I.N. Waterhouse − *School of Chemical Sciences, The University of Auckland, Auckland 1142, New Zealand*

Jingkun Yu − *College of Chemistry, Zhengzhou University, Zhengzhou 450000, China*

Hao Wang − *College of Chemistry, Zhengzhou University, Zhengzhou 450000, China*

Jinmeng Cai − *College of Chemistry, Zhengzhou University, Zhengzhou 450000, China*

Zhiyong Tang − *CAS Key Laboratory of Nanosystem and Hierarchical Fabrication, CAS Center for Excellence in Nanoscience, National Center for Nanoscience and Technology, Beijing 100190, China*

Bai Yang − *State Key Laboratory of Supramolecular Structure and Materials, College of Chemistry, Jilin University, Changchun 130012, China*

Author Contributions

The manuscript was written through contributions of all authors. All authors have given approval to the final version of the manuscript. ‡ H.S, and X.Y. contributed equally to this work.

Notes

The authors declare no competing financial interest.

ACKNOWLEDGMENT

The research presented in this work was supported by the National Natural Science Foundation of China (grant nos. 52122308, 51973200, 52202050, and 22305225) and the China Postdoctoral Science Foundation (2022TQ0286). G.I.N.W. acknowledge funding support from the Royal Society Te Apārangi (James Cook Research Fellowship) and the Ministry of Business Innovation and Employment (grant nos. C05X2007, UOCX2118).

ABBREVIATIONS

OER	oxygen evolution reaction;
ATR-SEIRAS	attenuated total reflectance surface-enhanced infrared absorption spectroscopy;
DEMS	differential electrochemical mass spectrometry;
DFT	density functional theory;
OPM	oxide path mechanism;
AEM-plus	enhanced adsorbate evolution mechanism;
PEMWEs	proton exchange membrane water electrolyzers;
HER	hydrogen evolution reaction;
OER	oxygen evolution reaction;
XRD	X-ray diffraction;
SEM	scanning electron microscopy;
TEM	transmission electron microscopy;

HAADF-STEM	high-angle annular dark-field scanning transmission electron microscopy;
XANES	X-ray absorption near-edge fine structure;
EXAFS	extended X-ray absorption fine structure;
WT	wavelet transform;
ECSA	electrochemically active surface area.

REFERENCES

(1) Chong, L.; Gao, G.; Wen, J.; Li, H.; Xu, H.; Green, Z.; Sugar, J. D.; Kropf, A. J.; Xu, W.; Lin, X.-M.; Xu, H.; Wang, L.-W.; Liu, D.-J., La- and Mn-doped cobalt spinel oxygen evolution catalyst for proton exchange membrane electrolysis. *Science* **2023,** *380* (6645), 609-616.

(2) Liu, R.-T.; Xu, Z.-L.; Li, F.-M.; Chen, F.-Y.; Yu, J.-Y.; Yan, Y.; Chen, Y.; Xia, B. Y., Recent advances in proton exchange membrane water electrolysis. *Chem. Soc. Rev.* **2023,** *52* (16), 5652-5683.

(3) Seitz, L. C.; Dickens, C. F.; Nishio, K.; Hikita, Y.; Montoya, J.; Doyle, A.; Kirk, C.; Vojvodic, A.; Hwang, H. Y.; Norskov, J. K.; Jaramillo, T. F., A highly active and stable $IrOx/SrIrO_3$ catalyst for the oxygen evolution reaction. *Science* **2016,** *353* (6303), 1011-1014.

(4) Zhu, M.; Zhao, C.; Liu, X.; Wang, X.; Zhou, F.; Wang, J.; Hu, Y.; Zhao, Y.; Yao, T.; Yang, L.-M.; Wu, Y., Single Atomic Cerium Sites with a High Coordination Number for Efficient Oxygen Reduction in Proton-Exchange Membrane Fuel Cells. *ACS Catal.* **2021,** *11* (7), 3923-3929.

(5) Grimaud, A.; Diaz-Morales, O.; Han, B.; Hong, W. T.; Lee, Y.-L.; Giordano, L.; Stoerzinger, K. A.; Koper, M. T. M.; Shao-Horn, Y., Activating lattice oxygen redox reactions in metal oxides to catalyse oxygen evolution. *Nat. Chem.* **2017,** *9* (5), 457-465.

(6) Li, A.; Kong, S.; Guo, C.; Ooka, H.; Adachi, K.; Hashizume, D.; Jiang, Q.; Han, H.; Xiao, J.; Nakamura, R., Enhancing the stability of cobalt spinel oxide towards sustainable oxygen evolution in acid. *Nat. Catal.* **2022,** *5* (2), 109-118.

(7) Wang, X.; Wan, X.; Qin, X.; Chen, C.; Qian, X.; Guo, Y.; Xu, Q.; Cai, W.-B.; Yang, H.; Jiang, K., Electronic Structure Modulation of RuO_2 by TiO_2 Enriched with Oxygen Vacancies to Boost Acidic O2 Evolution. *ACS Catal.* **2022,** *12* (15), 9437-9445.

(8) Dong, C.; Mu, R.; Li, R.; Wang, J.; Song, T.; Qu, Z.; Fu, Q.; Bao, X., Disentangling Local Interfacial Confinement and Remote Spillover Effects in Oxide–Oxide Interactions. *J. Am. Chem. Soc.* **2023,** *145* (31), 17056-17065.

(9) Wang, N.; Ou, P.; Miao, R. K.; Chang, Y.; Wang, Z.; Hung, S.-F.; Abed, J.; Ozden, A.; Chen, H.-Y.; Wu, H.-L.; Huang, J. E.; Zhou, D.; Ni, W.; Fan, L.; Yan, Y.; Peng, T.; Sinton, D.; Liu, Y.; Liang, H.; Sargent, E. H., Doping Shortens the Metal/Metal Distance and Promotes OH Coverage in Non-Noble Acidic Oxygen Evolution Reaction Catalysts. *J. Am. Chem. Soc.* **2023,** *145* (14), 7829-7836.

(10) Wen, Y.; Chen, P.; Wang, L.; Li, S.; Wang, Z.; Abed, J.; Mao, X.; Min, Y.; Dinh, C. T.; Luna, P. D.; Huang, R.; Zhang, L.; Wang, L.; Wang, L.; Nielsen, R. J.; Li, H.; Zhuang, T.; Ke, C.; Voznyy, O.; Hu, Y.; Li, Y.; Goddard Iii, W. A.; Zhang, B.; Peng, H.; Sargent, E. H., Stabilizing Highly Active Ru Sites by Suppressing Lattice Oxygen Participation in Acidic Water Oxidation. *J. Am. Chem. Soc.* **2021,** *143* (17), 6482-6490.

(11) Chen, Z.; Guo, L.; Pan, L.; Yan, T.; He, Z.; Li, Y.; Shi, C.; Huang, Z.-F.; Zhang, X.; Zou, J.-J., Advances in Oxygen Evolution Electrocatalysts for Proton Exchange Membrane Water Electrolyzers. *Adv. Energy Mater.* **2022,** *12* (14), 2103670.

(12) Du, K.; Zhang, L.; Shan, J.; Guo, J.; Mao, J.; Yang, C.-C.; Wang, C.-H.; Hu, Z.; Ling, T., Interface engineering breaks both stability and activity limits of RuO_2 for sustainable water oxidation. *Nat. Commun.* **2022,** *13* (1), 5448.

(13) Liu, Y.; Cai, L.; Ji, Q.; Wang, C.; Liu, Z.; Lv, L.; Tang, B.; Duan, H.; Hu, F.; Wang, H.; Li, N.; Sun, Z.; Yan, W., Operando Identification of Dual Active Sites in Ca_2IrO_4 Nanocrystals with Yttrium Substitutions Boosting Acidic Oxygen Evolution Reaction. *ACS Energy Lett.* **2022,** *7* (11), 3798-3806.

(14) Shi, Z.; Li, J.; Jiang, J.; Wang, Y.; Wang, X.; Li, Y.; Yang, L.; Chu, Y.; Bai, J.; Yang, J.; Ni, J.; Wang, Y.; Zhang, L.; Jiang, Z.; Liu, C.; Ge, J.; Xing, W., Enhanced Acidic Water Oxidation by Dynamic Migration of Oxygen Species at the Ir/Nb_2O_{5-x} Catalyst/Support Interfaces. *Angew. Chem. Int. Ed.* **2022,** *61* (52), e202212341.

(15) Zhang, X.-L.; Yu, P.-C.; Su, X.-Z.; Hu, S.-J.; Shi, L.; Wang, Y.-H.; Yang, P.-P.; Gao, F.-Y.; Wu, Z.-Z.; Chi, L.-P.; Zheng, Y.-R.; Gao, M.-R., Efficient acidic hydrogen evolution in proton exchange membrane electrolyzers over a sulfur-doped marcasite-type electrocatalyst. *Sci. Adv.* **2023,** *9* (27), eadh2885.

(16) Jin, H.; Choi, S.; Bang, G. J.; Kwon, T.; Kim, H. S.; Lee, S. J.; Hong, Y.; Lee, D. W.; Park, H. S.; Baik, H.; Jung, Y.; Yoo, S. J.; Lee, K., Safeguarding the RuO_2 phase against lattice oxygen oxidation during acidic water electrooxidation. *Energy Environ. Sci.* **2022,** *15* (3), 1119-1130.

(17) Lin, C.; Li, J.-L.; Li, X.; Yang, S.; Luo, W.; Zhang, Y.; Kim, S.-H.; Kim, D.-H.; Shinde, S. S.; Li, Y.-F.; Liu, Z.-P.; Jiang, Z.; Lee, J.-H., In-situ reconstructed Ru atom array on α-MnO_2 with enhanced performance for acidic water oxidation. *Nat. Catal.* **2021,** *4* (12), 1012-1023.

(18) Wu, Z.-Y.; Chen, F.-Y.; Li, B.; Yu, S.-W.; Finfrock, Y. Z.; Meira, D. M.; Yan, Q.-Q.; Zhu, P.; Chen, M.-X.; Song, T.-W.; Yin, Z.; Liang, H.-W.; Zhang, S.; Wang, G.; Wang, H., Non-iridium-based electrocatalyst for durable acidic oxygen evolution reaction in proton exchange membrane water electrolysis. *Nat. Mater.* **2023,** *22* (1), 100-108.

(19) Zhou, W.; Su, H.; Cheng, W.; Li, Y.; Jiang, J.; Liu, M.; Yu, F.; Wang, W.; Wei, S.; Liu, Q., Regulating the scaling relationship for high catalytic kinetics and selectivity of the oxygen reduction reaction. *Nat. Commun.* **2022,** *13* (1), 6414.

(20) Zhou, Y.; Sun, S.; Song, J.; Xi, S.; Chen, B.; Du, Y.; Fisher, A. C.; Cheng, F.; Wang, X.; Zhang, H.; Xu, Z. J., Enlarged Co-O Covalency in Octahedral Sites Leading to Highly Efficient Spinel Oxides for Oxygen Evolution Reaction. *Adv. Mater.* **2018,** *30* (32), 1802912.

(21) Shi, Z.; Wang, X.; Ge, J.; Liu, C.; Xing, W., Fundamental understanding of the acidic oxygen evolution reaction: mechanism study and state-of-the-art catalysts. *Nanoscale* **2020,** *12* (25), 13249-13275.

(22) Wang, Q.; Cheng, Y.; Tao, H. B.; Liu, Y.; Ma, X.; Li, D.-S.; Yang, H. B.; Liu, B., Long-Term Stability Challenges and Opportunities in Acidic Oxygen Evolution Electrocatalysis. *Angew. Chem. Int. Ed.* **2023,** *62* (11), e202216645.

(23) Wang, Y.; Yang, R.; Ding, Y.; Zhang, B.; Li, H.; Bai, B.; Li, M.; Cui, Y.; Xiao, J.; Wu, Z.-S., Unraveling oxygen vacancy site mechanism of Rh-doped RuO_2 catalyst for long-lasting acidic water oxidation. *Nat. Commun.* **2023,** *14* (1), 1412.

(24) Wang, Y.; Zhang, M.; Kang, Z.; Shi, L.; Shen, Y.; Tian, B.; Zou, Y.; Chen, H.; Zou, X., Nano-metal diborides-supported anode catalyst with strongly coupled $TaOx/IrO_2$ catalytic layer for low-iridium-loading proton exchange membrane electrolyzer. *Nat. Commun.* **2023,** *14* (1), 5119.

(25) Zhang, D.; Li, M.; Yong, X.; Song, H.; Waterhouse, G. I. N.; Yi, Y.; Xue, B.; Zhang, D.; Liu, B.; Lu, S., Construction of Zn-doped RuO_2 nanowires for efficient and stable water oxidation in acidic media. *Nat. Commun.* **2023,** *14* (1), 2517.

(26) An, L.; Yang, F.; Fu, C.; Cai, X.; Shen, S.; Xia, G.; Li, J.; Du, Y.; Luo, L.; Zhang, J., A Functionally Stable RuMn Electrocatalyst for Oxygen Evolution Reaction in Acid. *Adv. Funct. Mater.* **2022,** *32* (27), 2200131.

(27) He, J.; Li, W.; Xu, P.; Sun, J., Tuning electron correlations of RuO_2 by co-doping of Mo and Ce for boosting electrocatalytic water oxidation in acidic media. *Appl. Catal. B* **2021,** *298*, 120528.

(28) Niu, S.; Kong, X.-P.; Li, S.; Zhang, Y.; Wu, J.; Zhao, W.; Xu, P., Low Ru loading $RuO_2/(Co,Mn)_3O_4$ nanocomposite with modulated electronic structure for efficient oxygen evolution reaction in acid. *Appl. Catal. B* **2021,** *297*, 120442.

(29) Wang, C.; Geng, Q.; Fan, L.; Li, J.-X.; Ma, L.; Li, C.; Chen, S.; Huang, H.; Jiang, P.; Yang, K.; Diao, J.; Gong, S.; Liu, S.; Huang,

M.; Wang, H.; Chen, Q., Phase engineering oriented defect-rich amorphous/crystalline RuO_2 nanoporous particles for boosting oxygen evolution reaction in acid media. *Nano Research Energy* **2023,** *2* (2), e9120070.
(30) Harzandi, A. M.; Shadman, S.; Nissimagoudar, A. S.; Kim, D. Y.; Lim, H.-D.; Lee, J. H.; Kim, M. G.; Jeong, H. Y.; Kim, Y.; Kim, K. S., Ruthenium Core–Shell Engineering with Nickel Single Atoms for Selective Oxygen Evolution via Nondestructive Mechanism. *Adv. Energy Mater.* **2021,** *11* (10), 2003448.
(31) Li, M.; Wang, X.; Liu, K.; Zhu, Z.; Guo, H.; Li, M.; Du, H.; Sun, D.; Li, H.; Huang, K.; Tang, Y.; Fu, G., Ce-Induced Differentiated Regulation of Co Sites via Gradient Orbital Coupling for Bifunctional Water-Splitting Reactions. *Adv. Energy Mater.* **2023,** *13* (30), 2301162.
(32) Zhang, Y.; Zhao, S.; Feng, J.; Song, S.; Shi, W.; Wang, D.; Zhang, H., Unraveling the physical chemistry and materials science of CeO_2-based nanostructures. *Chem* **2021,** *7* (8), 2022-2059.
(33) Yang, Y.; Chai, Z.; Qin, X.; Zhang, Z.; Muhetaer, A.; Wang, C.; Huang, H.; Yang, C.; Ma, D.; Li, Q.; Xu, D., Light-Induced Redox Looping of a Rhodium/CexWO_3 Photocatalyst for Highly Active and Robust Dry Reforming of Methane. *Angew. Chem. Int. Ed.* **2022,** *61* (21), e202200567.
(34) Huang, J.; Sheng, H.; Ross, R. D.; Han, J.; Wang, X.; Song, B.; Jin, S., Modifying redox properties and local bonding of Co_3O_4 by CeO_2 enhances oxygen evolution catalysis in acid. *Nat. Commun.* **2021,** *12* (1), 3036.
(35) Zeng, S.-P.; Shi, H.; Dai, T.-Y.; Liu, Y.; Wen, Z.; Han, G.-F.; Wang, T.-H.; Zhang, W.; Lang, X.-Y.; Zheng, W.-T.; Jiang, Q., Lamella-heterostructured nanoporous bimetallic iron-cobalt alloy/oxyhydroxide and cerium oxynitride electrodes as stable catalysts for oxygen evolution. *Nat. Commun.* **2023,** *14* (1), 1811.
(36) Muravev, V.; Parastaev, A.; van den Bosch, Y.; Ligt, B.; Claes, N.; Bals, S.; Kosinov, N.; Hensen, E. J. M., Size of cerium dioxide support nanocrystals dictates reactivity of highly dispersed palladium catalysts. *Science* **2023,** *380* (6650), 1174-1179.
(37) Pei, Z.; Zhang, H.; Wu, Z.-P.; Lu, X. F.; Luan, D.; Lou, X. W., Atomically dispersed Ni activates adjacent Ce sites for enhanced electrocatalytic oxygen evolution activity. *Sci. Adv.* **2023,** *9* (26), eadh1320.
(38) Qin, Y.; Yu, T.; Deng, S.; Zhou, X.-Y.; Lin, D.; Zhang, Q.; Jin, Z.; Zhang, D.; He, Y.-B.; Qiu, H.-J.; He, L.; Kang, F.; Li, K.; Zhang, T.-Y., RuO_2 electronic structure and lattice strain dual engineering for enhanced acidic oxygen evolution reaction performance. *Nat. Commun.* **2022,** *13* (1), 3784.
(39) Liu, D.; Zeng, Q.; Hu, C.; Liu, H.; Chen, D.; Han, Y.; Xu, L.; Yang, J., Core–Shell CuPd@NiPd Nanoparticles: Coupling Lateral Strain with Electronic Interaction toward High-Efficiency Electrocatalysis. *ACS Catal.* **2022,** *12* (15), 9092-9100.
(40) Sarkar, S.; Ramarao, S. D.; Das, T.; Das, R.; Vinod, C. P.; Chakraborty, S.; Peter, S. C., Unveiling the Roles of Lattice Strain and Descriptor Species on Pt-Like Oxygen Reduction Activity in Pd–Bi Catalysts. *ACS Catal.* **2021,** *11* (2), 800-808.
(41) Wei, Z.; Ding, J.; Duan, X.; Chen, G.-L.; Wu, F.-Y.; Zhang, L.; Yang, X.; Zhang, Q.; He, Q.; Chen, Z.; Huang, J.; Hung, S.-F.; Yang, X.; Zhai, Y., Enhancing Selective Electrochemical CO_2 Reduction by In Situ Constructing Tensile-Strained Cu Catalysts. *ACS Catal.* **2023,** *13* (7), 4711-4718.
(42) Hao, J.; Zhuang, Z.; Hao, J.; Cao, K.; Hu, Y.; Wu, W.; Lu, S.; Wang, C.; Zhang, N.; Wang, D.; Du, M.; Zhu, H., Strain Relaxation in Metal Alloy Catalysts Steers the Product Selectivity of Electrocatalytic CO_2 Reduction. *ACS Nano* **2022,** *16* (2), 3251-3263.
(43) Wang, H.; Zhang, H.; Huang, Y.; Wang, H.; Ozden, A.; Yao, K.; Li, H.; Guo, Q.; Liu, Y.; Vomiero, A.; Wang, Y.; Qian, Z.; Li, J.; Wang, Z.; Sun, X.; Liang, H., Strain in Copper/Ceria Heterostructure Promotes Electrosynthesis of Multicarbon Products. *ACS Nano* **2023,** *17* (1), 346-354.
(44) Jin, H.; Liu, X.; An, P.; Tang, C.; Yu, H.; Zhang, Q.; Peng, H.-J.; Gu, L.; Zheng, Y.; Song, T.; Davey, K.; Paik, U.; Dong, J.; Qiao, S.-Z., Dynamic rhenium dopant boosts ruthenium oxide for durable oxygen evolution. *Nat. Commun.* **2023,** *14* (1), 354.
(45) Wang, K.; Wang, Y.; Yang, B.; Li, Z.; Qin, X.; Zhang, Q.; Lei, L.; Qiu, M.; Wu, G.; Hou, Y., Highly active ruthenium sites stabilized by modulating electron-feeding for sustainable acidic oxygen-evolution electrocatalysis. *Energy Environ. Sci.* **2022,** *15* (6), 2356-2365.
(46) Zhu, W.; Yao, F.; Cheng, K.; Zhao, M.; Yang, C.-J.; Dong, C.-L.; Hong, Q.; Jiang, Q.; Wang, Z.; Liang, H., Direct Dioxygen Radical Coupling Driven by Octahedral Ruthenium–Oxygen–Cobalt Collaborative Coordination for Acidic Oxygen Evolution Reaction. *J. Am. Chem. Soc.* **2023,** *145* (32), 17995-18006.
(47) Shi, Z.; Li, J.; Wang, Y.; Liu, S.; Zhu, J.; Yang, J.; Wang, X.; Ni, J.; Jiang, Z.; Zhang, L.; Wang, Y.; Liu, C.; Xing, W.; Ge, J., Customized reaction route for ruthenium oxide towards stabilized water oxidation in high-performance PEM electrolyzers. *Nat. Commun.* **2023,** *14* (1), 843.
(48) Su, H.; Zhou, W.; Zhou, W.; Li, Y.; Zheng, L.; Zhang, H.; Liu, M.; Zhang, X.; Sun, X.; Xu, Y.; Hu, F.; Zhang, J.; Hu, T.; Liu, Q.; Wei, S., In-situ spectroscopic observation of dynamic-coupling oxygen on atomically dispersed iridium electrocatalyst for acidic water oxidation. *Nat. Commun.* **2021,** *12* (1), 6118.

For Table of Contents Only